Available online at www.sciencedirect.com

ScienceDirect

Advances in Space Research 56 (2015) 2345–2355

ADVANCES IN SPACE RESEARCH (a COSPAR publication)

www.elsevier.com/locate/asr

Effects of atmospheric correction of Landsat imagery on lake water clarity assessment

Matias Bonansea [a,b,*], C. Ledesma [b], C. Rodríguez [b], L. Pinotti [a], M. Homem Antunes [c]

[a] Consejo Nacional de Investigaciones Científicas y Técnicas (CONICET), Ruta Nacional 36 Km 601, (5800) Río Cuarto, Córdoba, Argentina
[b] Departamento de Estudios Básicos y Agropecuarios, Facultad de Agronomía y Veterinaria (FAyV), Universidad Nacional de Río Cuarto (UNRC), Argentina
[c] Departamento de Ingeniería, Universidad Federal Rural de Río de Janeiro, IT/DE, Br 465 km 7, Seropédica, RJ, Brazil

Received 14 October 2014; received in revised form 29 July 2015; accepted 11 September 2015
Available online 25 September 2015

Abstract

Empirical relationships between Landsat data and water clarity expressed in terms of Secchi disk transparency (SDT) have been widely used for monitoring and assessment of water quality. The atmosphere affects differently sensor bands depending on the waveband, thus affecting the relationships obtained from top-of-atmosphere reflectance. The objective of this study was to evaluate whether the reliability of water clarity can be improved applying atmospheric correction of Landsat imagery. Further, a general predictive algorithm to determine water clarity in the reservoir was developed. Samples of SDT were taken from Río Tercero reservoir (Argentina). Landsat images were atmospheric corrected using the 6S code. Estimated values of SDT with and without atmospheric correction were compared for their differences. Results suggested that atmospheric corrected values of Landsat band 3 and the ratio 1/3 proved to be the best predictor of water clarity in the reservoir ($R^2 = 0.84$). Using the 6S code we demonstrate the usefulness of atmospheric correction to Landsat data since water clarity algorithm using surface reflectance was more reliable than the top-of atmosphere reflectance model.

Keywords: Atmospheric correction; Landsat; Reservoir; 6S model; Water clarity

1. Introduction

Decision makers are demanding new tools for monitoring and assessment of water quality. Satellite remote sensing reduces expensive and labor-intensive *in-situ* measurements by providing a spatially and temporally continuous coverage of environmental processes (Chernetskiy et al., 2009; Karakaya et al., 2011; Trivero et al., 2013). Among several satellite systems that have been used for water quality monitoring, the Landsat system is particularly useful for assessment of inland lakes (Kloiber et al., 2002a; Olmanson et al., 2008; Matthews, 2011). Most techniques for remote sensing of water quality construct reliable empirical relationship between Landsat data and ground observations of water quality parameters, including chlorophyll and phycocyanin concentrations (Vincent et al., 2004; Fernandez et al., 2012; Tebbs et al., 2013), water clarity expressed in terms of Secchi disk transparency (SDT) (Zhao et al., 2011; McCullough et al., 2012a), total suspended sediments (Kulkarni, 2011; Bonansea and Fernandez, 2013; Fernandez et al., 2014), among others. In this study, we focus on SDT estimation due to its simplicity and relatively low cost. Besides this parameter, which is widely used and a common metric of lake water quality, has strong ecological and economic implications,

* Corresponding author at: Consejo Nacional de Investigaciones Científicas y Técnicas (CONICET), Universidad Nacional de Río Cuarto (UNRC), Ruta Nacional 36 km 601, (5800) Río Cuarto, Córdoba, Argentina. Tel.: +54 358 46 76512.
E-mail address: mbonansea@ayv.unrc.edu.ar (M. Bonansea).

http://dx.doi.org/10.1016/j.asr.2015.09.018
0273-1177/

being a highly useful indicator of trophic status and ecosystem health (Sriwongsitanon et al., 2011; Zhao et al., 2011; McCullough et al., 2012b; Chao Rodríguez et al., 2014). According to Domínguez Gómez et al. (2009), the assessment of water clarity has a crucial impact on water quality monitoring because it shows, in a global way, all the components that can be found in water and the many interactions existing among them.

To relate Landsat data and water clarity most studies use classical regression models between radiation data collected by satellites and *in-situ* SDT measurements (Olmanson et al., 2008; Matthews, 2011). However, the electromagnetic radiation signal collected by satellites in the solar spectrum is modified by scattering and absorption by gases and aerosols while traveling through the atmosphere from the Earth surface to the sensor (Song et al., 2001). For rectifying these scattering and absorption effects, which depend on the wavelength of the sensor system and can vary considerably in both space and time, atmospheric correction are essential to satellite remote sensing (Sharma et al., 2009). If atmospheric effects can be removed properly, information from multitemporal data sets over regions with variable aerosol loading can be sensibly compared (Takashima and Masuda, 2000).

A number of radiative transfer codes (RTCs) have been developed to correct for atmospheric effects in satellite imagery (Kneizys et al., 1988; Berk et al., 1989; Rahman and Dedieu, 1994; Zhao et al., 1999). Among these models the 6S (Second Simulation of Satellite Signal in the Solar Spectrum) code (Vermote et al., 1997) was mainly developed for the purpose of making atmospheric corrections in the short wavelength region, and 6S better handles atmospheric scattering during radiative transfer than other models (Zhao et al., 2000). Effectiveness of 6S code for correcting satellite images affected by atmospheric factors was assessed by several researchers, proving that 6S model can be effectively used in satellite images with different resolutions. Zhao et al. (2000) found significant improvements in albedo after atmospheric corrections were applied on NOAA/AVHRR and Landsat TM data. Tachiiri, 2005 using the 6S code for correcting NDVI images from NOAA/AVHRR data found considerable increase in the range of Normalized Difference Vegetation Index (NDVI) after atmospheric correction. Vermote and Saleous (2006) demonstrated utility of the 6S code for atmospheric correction for MODIS visible to middle infrared land surface data. Sharma et al. (2009) concluded that corrected reflectance data of IRS-P6 AWIFS satellite better separated ground features such as water bodies and crop fields compared to uncorrected data. Other examples of the 6S code and its applications can be found in Ouaidrari and Vermote (1999) and Masek et al. (2006).

Although most of the studies of water quality estimation by remote sensing and its improvements after atmospheric correction were carried out for the northern hemisphere, little has been done to develop appropriate assessment of water clarity in the southern hemisphere. Thus, the objective of this study was to evaluate whether the reliability of water clarity can be improved applying atmospheric correction of Landsat imagery with the 6S radiative transfer model in Río Tercero reservoir (Argentina). The 6S radiative transfer model was chosen for this study, because it is a physically based model that is not optimized on one specific satellite scene, test site, and object class. Further, using different statistical techniques a general predictive algorithm to determine water clarity in the reservoir was developed. The predictive model was used to generate a map which provided rich information on pattern of SDT in the water body, allowing the discrimination of changes in water clarity and providing new insights that can greatly benefit monitoring efforts of aquatic ecosystems. Estimated values of SDT with and without atmospheric correction were compared for their differences. The procedure presented here could become an independent, low additional training and low cost measurement tool for water management authorities and decision makers not only for the studied reservoir, but also for aquatic systems at a regional scale.

2. Methodology

2.1. Study area

Río Tercero Reservoir (32° 11′S, 64° 23′W) is located in the province of Córdoba, Argentina (Fig. 1). This reservoir, which is the largest artificial reservoir in the province, has an area of 46 km^2, a volume of 10^7 m^3 and maximum and mean depths of 46.5 and 12.2 m, respectively (Mariazzi et al., 1992; Ledesma et al., 2013).

The reservoir has multiple purposes such as water supply, power generation, flood control, irrigation, tourism and recreational activities (Lamaro et al., 2013; Bonansea et al., 2015). In 1986 a nuclear power plant (Central Nuclear Embalse, CNE), was installed. Water for cooling the nuclear reactor is taken from the middle section of the reservoir. In the cooling system water temperature increases 7.0 °C and is returned to the reservoir by a 5-km long open-sky channel (Mariazzi et al., 1992).

2.2. Field campaigns

As part of a monitoring program, several physical, chemical and biological properties of reservoir water quality have been surveyed. Water sampling was conducted on May 18, 2004; September 24, 2006; September 07, 2010; and November 10, 2010. Nine sampling sites, distributed nearly uniformly across the reservoir were sampled (Fig. 1). Coordinates of sample sites were recorded using a GPS device. Water clarity was estimated in the field by measuring SDT using a standard 20 cm diameter Secchi disk painted in black/white quarters. Because of its simplicity, the Secchi disk has been widely used for this purpose (Kloiber et al., 2002b). SDT is a measure of how deep a person can see into the water and is one of the three most

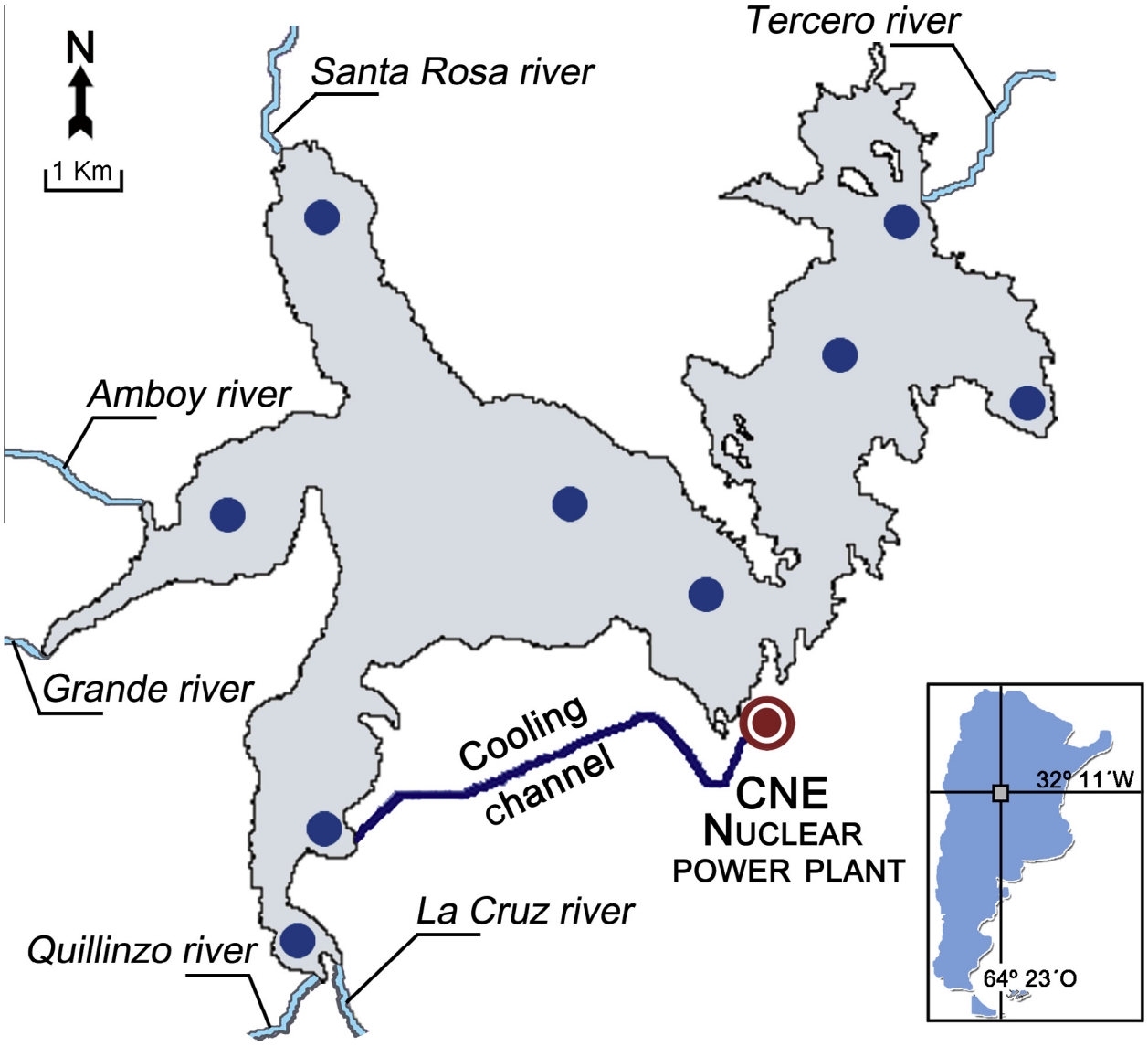

Fig. 1. Study area and sampling sites.

commonly used indicators of trophic state for inland water bodies (Zhao et al., 2011).

2.3. Satellite data

The Landsat series of satellite missions has collected imagery of the Earth's surface since 1972, providing an unparalleled record of the status and dynamics of Earth (Cohen and Goward, 2004). The Landsat 7 Enhanced Thematic Mapper (ETM+) satellite, launched in 1999, is equipped with a multi-spectral scanning equipment, which operates on seven spectral bands located between the visible (band 1–3) and infrared regions (band 4, 5 and 7) of the spectrum and an additional 15 m panchromatic band (band 8). The spatial resolution is 30 m for the visible through middle infrared channels and 60 m for thermal infrared band (band 6), allowing the detection of small scale spatial variability across a reservoir surface (Xu et al., 2013). This sensor present a revisit time of 16 days and a radiometric resolution of 256 digital numbers (DN) (Oguro et al., 2003; Loveland and Dwyer, 2012).

The criteria for image selection were: existing *in-situ* data in ±4 days to the satellite passes (time window) obtaining reasonable results for empirical relationships between SDT and Landsat imagery; no heavy rainfall prior to the image data to minimize the effects of changes in water surfaces that disturb the estimates; 0% haze or cloud cover when possible. To detect haze and cloud cover, which affect spectral-radiometric responses and cause erroneous results, an RGB band combination (1, 6, 6) was used (Olmanson et al., 2008). The selected criteria are in agreement with different authors (Kloiber et al., 2002b; Sriwongsitanon et al., 2011; Tebbs et al., 2013). Thus, from the pool of suitable images, we selected four Landsat ETM + scenes (Path: 229; Row: 82) dated May 14, 2004; September 28, 2006; September 07, 2010; and November 10, 2010

that were downloaded from USGS Global Visualization Viewer (http://glovis.usgs.gov/). The images were Level 1T processed, meaning that they had undergone geometric calibration and terrain calibration (Irish, 1998). Thus, no further geometric corrections were needed.

2.4. Image pre-processing

The uncalibrated DN of ETM+ images were converted to at-sensor spectral radiance (L_λ) using Eq. (1) (Huang et al., 2002):

$$L_\lambda = G_{rescale} * DN + B_{rescale} \quad (1)$$

where $G_{rescale}$ is the band-specific rescaling gain factor and $B_{rescale}$ is the band-specific rescaling bias factor. Table 1 summarizes the spectral range and post-calibration dynamic ranges for the ETM+ sensor. According to Chander et al. (2009), ETM+ images are acquired in either a low-or high-gain state to maximize the sensors' 8-bit radiometric sensitivity and dynamic range without saturating the detectors. The mode in which energy is stored in each band can be found in the Level 1T product header file or retrieved from the USGS Global Visualization Viewer online interface under the respective scene metadata.

To reduce variability between scenes, allowing better image comparison, the spectral radiance was converted to the top-of-atmosphere reflectance (ρ_{TOA}), according to Eq. (2) (Irish, 1998):

$$\rho_{TOA} = \frac{\pi * L_\lambda * d^2}{ESUN_\lambda * \cos(\theta_Z)} \quad (2)$$

where d is the Earth–Sun distance in astronomical units, $ESUN_\lambda$ is the mean solar exoatmospheric irradiance for each band (values for different bands shown in Table 1) and cos (θ_Z) is the solar zenith angle in degrees, which is typically stored in the Level 1T product header file of the respective scene. The Earth–Sun distance (d) has a relationship to the Julian day (Dy) of the satellite data acquisition as shown in Eq. (3).

$$d = 1 - [0.01672 * \cos(0.9856(Dy - 4))] \quad (3)$$

Atmospheric correction was carried out using the 6S radiative transfer model. Using the 6S code, the surface reflectance free from atmospheric reflectance (R) is calculated by Eq. (4) (Mahiny and Turner, 2007).

$$R = \frac{A * \rho_{TOA} + B}{1 + \gamma(A * \rho_{TOA} + B)} \quad (4)$$

where $A = 1/\alpha\beta$, $B = -\rho/\beta$, α is the global gas transmittance, β is the total scattering transmittance, ρ is the atmospheric reflectance, and γ is the spherical albedo. These parameters are constants generated internally from running the model.

Homem Antunes (http://www.ltid.inpe.br/dsr/mauro/6s/download_6s.html) developed a version of the 6S code in which the minimum data set needed to run the model is date and universal time of image acquisition, center latitude and longitude, sensor type, terrain elevation, meteorological visibility, and atmospheric and aerosol model. The values of center latitude and longitude, date and time of image acquisition were extracted from the Level 1T product header file. Measures of meteorological visibility and terrain elevation were provided by the Argentine National Weather Service (http://www.smn.gov.ar). To define the atmospherical and aerosol model, we used the standard models proposed by 6S code (the mid-latitude atmospheric model and the continental aerosol model). 6S code then automatically estimates the input parameters of solar zenith angle and solar azimuthal angle, satellite zenith angle, water vapor, ozone, aerosol optical depth, and sensor height (Table 2). Using the input data and the embedded features, the model internally produces variables to assess the surface reflectance (Mahiny and Turner, 2007).

In this study we have not used the thermal infrared band because this spectral band is not suitable to be used for developing relationships between *in-situ* sampled data versus Landsat data (Sriwongsitanon et al., 2011). This band, which measures the amount of infrared radiant flux emitted from Earth's surface, is normally used in measuring surface temperature or in locating geothermal activity and thermal inertia mapping (Barsi et al., 2005; Mukherjee et al., 2014).

After 2003 the Scan Line Corrector (SLC) of ETM+ failed and as a result the images contain lines of missing data (Tebbs et al., 2013). Using a methodology adapted from the SLC Gap-Filled Products, Phase One

Table 1
ETM+ spectral ranges, post-calibration dynamic ranges and mean exoatmospheric solar irradiance ($ESUN_\lambda$).

Band	Spectral range (nm)	$G_{rescale}$ (W/(m^2 sr μg)/DN)		$B_{rescale}$ (W/(m^2 sr μg))		$ESUN_\lambda$ (W/(m^2 μg))
		Low gain	High gain	Low gain	High gain	
1	0.452–0.514	1.180709	0.778740	−7.38	−6.98	1997.0
2	0.519–0.601	1.209843	0.798819	−7.61	−7.20	1812.0
3	0.631–0.692	0.942520	0.621654	−5.94	−5.62	1533.0
4	0.772–0.898	0.969291	0.639764	−6.07	−5.74	1039.0
5	1.547–1.748	0.191220	0.126220	−1.19	−1.13	230.8
6	10.31–12.36	0.067087	0.037205	−0.07	3.16	–
7	2.065–2.346	0.066496	0.043898	−0.42	−0.39	84.9
PAN	0.515–0.896	0.975591	0.641732	−5.68	−5.34	1362.0

Table 2
Input parameters for 6S radiative transfer model application.

Parameters	May 14, 2004	September 28, 2006	September 7, 2010	November 10, 2010
Solar zenith angle (°)	46.01	42.86	49.83	31.11
Solar azimuthal angle (°)	57.73	52.36	46.44	68.89
Satellite zenith angle (°)	0.25	0.22	0.28	0.12
Aerosol model	Continental	Continental	Continental	Continental
Aerosol optical depth	0.3740	0.4004	0.4321	0.4004
Ozone (cm-atm)	0.317	0.319	0.395	0.319
Water vapor (g/cm^2)	2.145	2.93	0.853	2.93
Sensor height (km)	705	705	705	705
Terrain elevation (km)	0.64	0.64	0.64	0.64

Methodology article (USGS, 2004), SLC failure was corrected predicting the best closest value of the missing pixels. To delineate the lake surface masks, producing "water-only" images and isolating anomalously pixels that do not belong to the reservoirs, the Normalized Difference Water Index (NDWI) algorithm proposed by McFeeters (1996) was applied. The NDWI can be used successfully in delineating water bodies and monitoring the water area changes (Ji et al., 2009).

2.5. Model development

As the locations of sampling points were georreferenced, it was possible to compare matchups between field data and corresponding ETM+ data. A median value from a 3×3 pixel box centered at an *in-situ* measurement site was used to filter sensor and algorithm noise (Hu et al., 2001). In the context of this study, SDT values were log-transformed to obtain stronger correlations to Landsat data. A log-transformed water quality parameter relationship to Landsat data is better than a relationship in the original domain (Brezonik et al., 2005; Sriwongsitanon et al., 2011). We chose not to employ preconceived notions concerning the best band or band ratio for estimating water clarity in the reservoir. Thus, to identify which spectral band or band ratio was the best predictor of SDT, Pearson correlation coefficients and step-wise multiple regression analysis were carried out between measured SDT data versus atmospherically uncorrected and corrected ETM+ reflectance values. The selected bands were used to generate a model to estimate water clarity in the reservoir. Standard regressions assumptions were verified graphically and statistically. To study the adequacy of the models we used Shapiro Wilks's test ($p > 0.05$) to prove assumption of normality. Levene's test ($p > 0.05$) was used to verify homogeneity of variances. Using the same dataset that in the model generation step, simple regression analysis was made to evaluate the correlation between estimated versus observed SDT data. The best SDT models obtained from TOA reflectance values and surface reflectance values were then applied to the November 10, 2010 ETM+ image, obtaining qualitative maps to characterize water clarity in the reservoir. Maps of the spatial distribution of simulated errors, calculated as the difference between estimated and observed SDT data, were also provided.

3. Results and discussion

Table 3 shows the results of Pearson correlation coefficients between ln(SDT) versus atmospherically uncorrected and corrected ETM+ spectral band and band ratio. Although all possible band ratio combinations were considered, we only show ratios between ETM+ band 1 to 4. According to Brezonik et al. (2005) suspended particles cause an increase in the measured response for Landsat band 1–4. This agrees with Matthews (2011) who suggests that the optically active water constituents and water itself, all have an impact on the optical signature of water in the visible and near-infrared (NIR) wavelengths (band 1–4). Band ratios that included bands of the middle to far infrared regions (band 5 and 7) were not shown because these bands, which showed no evidence of significant association with ln(SDT) data ($p > 0.05$ for both cases), are generally useful for vegetation and soil moisture studies and for discriminating between rock and mineral types (Sriwongsitanon et al., 2011).

As we expected, SDT was correlated with brightness in the visible and NIR of the spectrum, and not well correlated with brightness in the middle to far infrared regions. Results show that ETM+ band 3 was negative correlated with ln(SDT). Matthews (2011) suggests that the negative correlation with this spectral band may be explained by the direct positive correlation between reflectance in this region of the spectrum and gross particulate load inducing particulate scattering. Therefore, as water clarity decreases, brightness in band 3 usually increases. In addition, the Pearson correlation coefficient (r) between *in-situ* data and band 3 was higher when the 6S code was applied ($r = -0.69$ for uncorrected data, and $r = -0.83$ for corrected data). The low association between ln(SDT) and bands 1 and 2 could be associated with the low number of sampling sites. Negative correlation between ln(SDT) and corrected ETM+ band 4 ($r = -0.64$) was also observed. Although absorbance in water increases sharply in this band, increased reflectance by suspended particles still can be detected (Dekker and Peters, 1993; Brezonik et al., 2005). Previous investigations have suggested that

Table 3
Pearson correlation coefficients between log-transformed SDT versus ETM+ spectral band and band ratio. Italic shows correlations which were significant ($p > 0.05$) and bold indicates absolute correlation values higher than 0.50.

Band			Band ratio					
	U	C		U	C		U	C
1	−0.41	−0.46	1/2	***0.54***	***−0.56***	3/1	***−0.71***	***−0.72***
2	−0.45	−0.49	1/3	***0.74***	***0.76***	3/2	***−0.57***	***−0.55***
3	***−0.69***	***−0.83***	1/4	0.32	0.21	3/4	0.15	−0.03
4	−0.41	***−0.64***	2/1	***−0.57***	***−0.57***	4/1	−0.41	−0.17
5	−0.42	−0.24	2/3	***0.53***	***0.51***	4/2	−0.38	0.19
7	−0.08	−0.18	2/4	0.26	0.04	4/3	−0.18	0.12

U = uncorrected atmospheric effect; C = corrected atmospheric effect.

band ratios provide useful relationships (Lavery et al., 1993; Kloiber et al., 2002a). We found that the ratio 1/3 showed the higher Pearson correlation coefficients with ln (SDT) ($r = 0.74$ for uncorrected ratio, and $r = 0.76$ for corrected ratio). Correlations between ln(SDT) and band ratios 3/1, 1/2, 2/1, 2/3, and 3/2 were also significant and consistent ($p > 0.05$ and $r < 0.50$).

Results found in the Pearson correlation analysis agree with the regression analysis. Thus, using step-wise multiple regression analysis, we confirmed that the best estimated responses between *in-situ* SDT versus TOA reflectance and surface reflectance were given by Eqs. (5) and (6), respectively. The combination of these factors provided reasonable predictions of SDT for the ETM+ images used in this study.

$$\ln(SDT) = -2.28 - 2.42 * Band3_{\rho_{TOA}} + 1.48 * \left(\frac{Band1_{\rho_{TOA}}}{Band3_{\rho_{TOA}}}\right) \quad (5)$$

$$\ln(SDT) = 1.25 - 0.44 * Band3_{R} + 0.11 * \left(\frac{Band1_{R}}{Band3_{R}}\right) \quad (6)$$

where $Band3\rho_{TOA}$ and $Band3_R$ are the top-of-atmosphere reflectance and surface reflectance for ETM+ band 3, respectively. $Band1\rho_{TOA}/Band3\rho_{TOA}$ and $Band1_R/Band3_R$ are the TOA and surface reflectances for ratio between band 1 and 3.

According to Matthews (2011) there are a large number of studies using Landsat to retrieve SDT, and most of these use linear regressions of single bands or band ratios. Different studies suggest that SDT can be estimated form different combinations of Landsat bands 1 to 4 (Doña et al., 2014; Sriwongsitanon et al., 2011). In this sense, Chao Rodríguez et al. (2014), generated an algorithm to predict SDT relating Landsat 1 and 2. Cózar et al. (2005), found that SDT could be estimated with a combination of band 1, 3 and 4. Onderka and Pekárová (2008) used ETM+ band 4 to estimate the spatial patterns of suspended particulate matter in Danube river (Slovakia). Matthews (2011) suggests that there are some examples that use Landsat band 2 to estimate SDT (Lathrop and Lillesand, 1986; Doña et al., 2014), although there are few recent examples of this. Zhao et al. (2011) suggest that the differences in band selection to estimate SDT may be related to differences in image quality or may depend on the limnological properties of the water body. Sriwongsitanon et al. (2011), found that Landsat band ratios 3/1 and 2/3 are the most suitable relationship for estimation of SDT in Bung Boraphet, the largest lake in Central Thailand. In our study, Landsat band 3 plus the ratio 1/3 provided strong predictive relationship with SDT in Río Tercero reservoir. Several investigators had success with similar relationship. The same band combination was used by Lavery et al. (1993) studying an estuarine system in the western of Australia. Hellweger et al. (2004) found that TM band 3 provided a strong relationship to SDT. McCullough et al. (2012a) used TM bands 1 and 3 to predict SDT for Maine lakes, United States. According to Matthews (2011), the ratio between TM bands 1 and 3 is particularly common to estimate lake water clarity. Lathrop (1992) and Cox et al. (1998) suggest that ratio 1/3 is a strong predictor of SDT. Kloiber et al. (2002b) and Brezonik et al. (2005) used Landsat band 1 plus ratio 1/3 to predict SDT with high accuracy. Similar results were found by Olmanson et al. (2008) studying a series of lakes in Minnesota (United States) and Zhao et al. (2011) in Taihu lake, China.

Comparing the SDT models created with and without atmospheric corrections, we found that coefficient of determination (R^2) was higher for 6S corrected data ($R^2 = 0.84$) than for the uncorrected TOA reflectance ($R^2 = 0.79$), suggesting that surface reflectance data obtained after atmospheric correction of satellite sensor imagery offers some advantages compared with usage of the uncorrected data. Although both model showed an acceptable root mean square error (RMSE), the lower RMSE found in the corrected model (RMSE = 0.20 m), proves that this algorithm is more robust than the best model derived from uncorrected ETM+ data (RMSE = 0.24 m).

Although we could have created the most suitable SDT algorithm between the selected band combination and *in-situ* data for each studied event, obtaining more accurate results of SDT than the provided by Eq. (6) as shown in Table 4, we create a general algorithm for predicting SDT in Río Tercero reservoir which could be used as a standardized procedure to assess detailed spatio-temporal distribution of water clarity, strengthening the results for water management authorities and decision makers in the management of aquatic systems.

Table 4
Regression parameters and coefficients for the most appropriate relationships between the selected band combination and *in-situ* data for each studied event.

Sampling date	Image date	Atmospheric effect	Regression equation coefficients			R^2	RMSE (m)
			Constant	ETM+ 3	ETM+ 1/3		
May 18, 2004	May 14, 2004	Uncorrected	−5.48	38.40	2.19	0.86	0.01
		Corrected	0.21	0.23	0.37	0.96	0.05
September 24, 2006	September 28, 2006	Uncorrected	−3.90	8.60	2.15	0.90	0.20
		Corrected	0.84	−0.35	0.34	0.88	0.20
September 7, 2010	September 7, 2010	Uncorrected	6.19	−76.90	0.59	0.87	0.07
		Corrected	3.36	−1.77	−0.30	0.89	0.11
November 10, 2010	November 10, 2010	Uncorrected	10.13	−22.58	−0.98	0.83	0.10
		Corrected	1.89	−0.89	0.04	0.84	0.10

Regressions between ETM+ estimates versus *in-situ* measurements of ln(SDT) generated with Eqs. (5) and (6) are plotted in Fig. 2. The good fit between estimated and observed water clarity measurement using surface reflectance values and the better agreement between the gradient and intercept of the regression line found in this plot (Fig. 2b) indicates the high predictive capacity of this model ($R^2 = 0.85$).

Fig. 3 compares the spatial distribution of SDT in Río Tercero reservoir applying the best SDT algorithms without atmospheric correction against corrected values to the November 10, 2010 ETM+ image. Ground measures of SDT in Río Tercero reservoir ranged from 1.6 to 6.0 m, with a mean value of 3.7 m. Satellite estimated SDT values varied between <0.5 to about 5.6 m, with a mean value of 3.2 m in the uncorrected image. The values of water clarity in the corrected image varied between <0.5 to 6.5 m, with a mean value of 3.8 m. Visual interpretation of the maps (Fig. 3a) clearly shows increase in contrast after atmospheric correction was applied. It is clear that differences between water clarity categories that were less distinguishable in uncorrected map appear clearly after atmospheric correction. Thus atmospheric correction can be used to increase separability between water clarity categories.

The analysis of the spatial distribution of simulation error maps (Fig. 3b) indicates that ground measures of SDT and estimated values of SDT using surface reflectance data follow a similar pattern and showed little difference, suggesting a better estimation of water clarity than using TOA reflectance. Both maps show that the central region of the reservoirs presented the lower difference between simulated and observed data, whereas the higher simulation errors were located near the shores. This could be related with the effect of the bottom (Bonansea and Fernandez 2013). Considering the uncertainty in human estimation error associated with the visual assessment of water clarity based on Secchi disks, the RMSE obtained in both maps is quite satisfactory (RMSE = 0.21 m for corrected data, and RMSE = 0.24 m for uncorrected data).

Results of this study suggest that over mid-latitude region, atmospheric correction plays an important role in deriving quantitative information from satellite data to estimate reservoir water clarity. Applying the 6S model

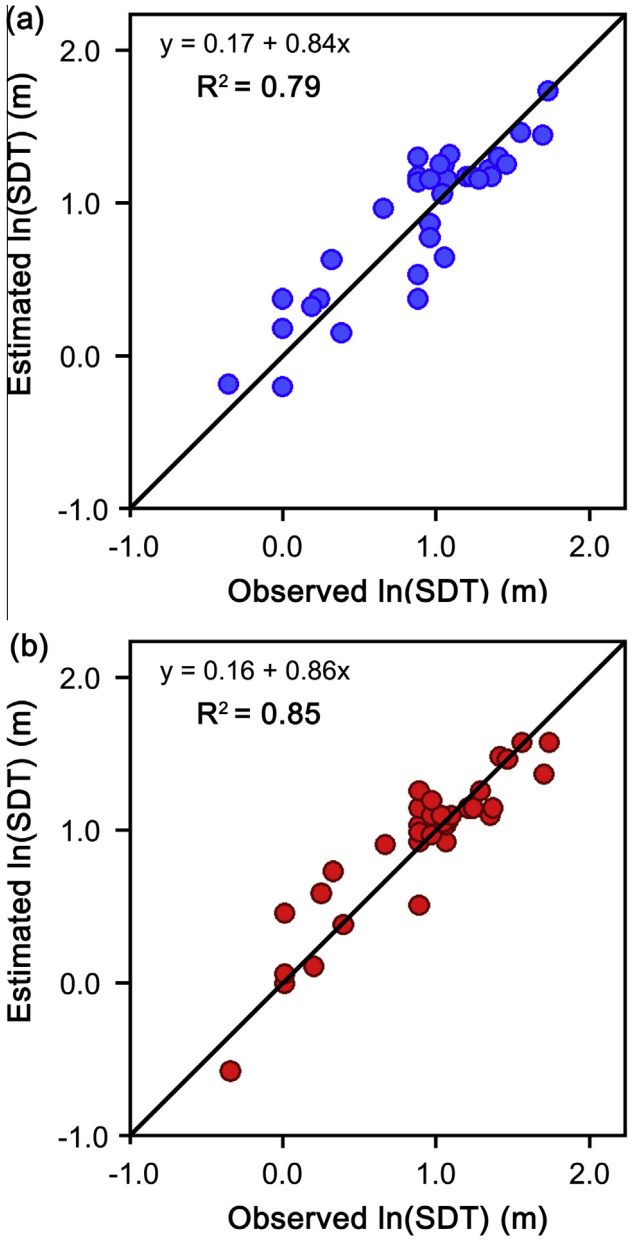

Fig. 2. Scatter plot of observed ln(SDT) versus Landsat-estimated using (a) top-of-atmosphere reflectance and (b) surface reflectance values with 1:1 fit line.

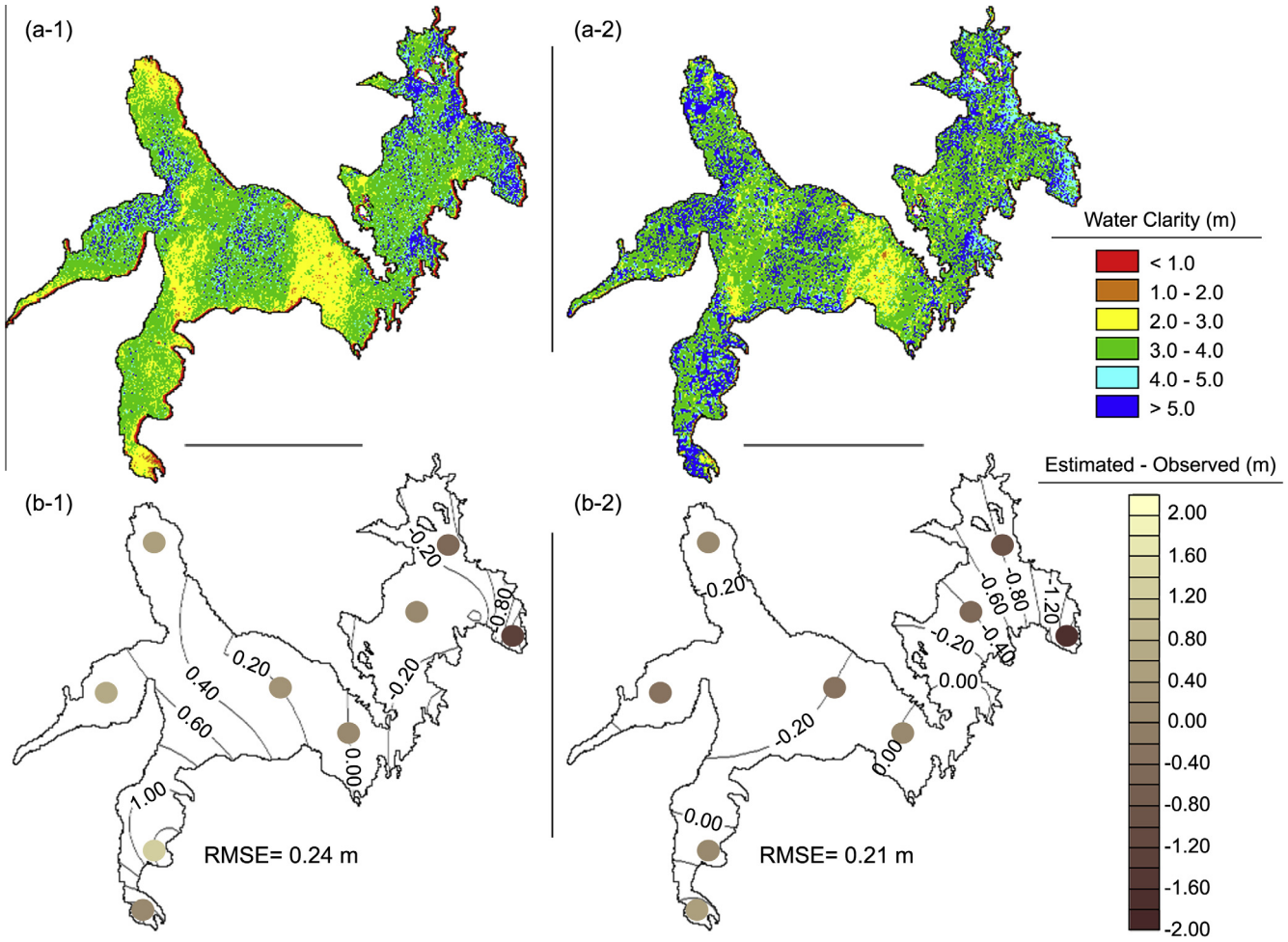

Fig. 3. (a) Estimated water clarity maps, and (b) spatial distribution of simulated errors using (1) top-of-atmosphere reflectance and (2) surface reflectance values obtained from November 10, 2010 ETM+ image.

for atmospheric correction to the ETM+ images brought about differences in surface reflectance of each band comparing with TOA values of all bands. This was confirmed in Table 5 which compares ETM+ band values with and without atmospheric correction. In visible bands (band 1, 2 and 3), the corrected reflectance values were lower than the uncorrected reflectance values. The average reflectance values of these bands reduced around 62%, 37% and 26% compared to the uncorrected values, respectively for the first image, around 37, 3 and 19%, respectively for the second image, around 61%, 22% and 14%, respectively for the third image, and around 40%, 11% and 11%, respectively for the November 10, 2010 image. Using surface reflectance data we could reduce the effects of atmospheric Rayleigh and aerosol scattering, which provide image additive effects in visible bands. According to Sriwongsitanon et al. (2011), aerosol scattering which is stronger in the shorter solar wavelengths where the particle size is similar to the radiation wavelength, increases the apparent surface reflectance over dark surfaces. Thus, the 6S atmospheric correction model can remove additive effects in the visible bands thereby reducing their TOA reflectance values. This is supports by Sharma et al. (2009) who suggest that correcting the atmospheric effects tends to decrease the reflectance values and introduce significant variations in the spectral reflectance in atmospherically corrected versus uncorrected spectral bands. Comparisons of water clarity derived from Landsat data before and after atmospheric correction suggested that SDT values estimated with the 6S code were close to ground measured values. Thus, correcting the atmospheric effects of Landsat data tend to obtain more reliable and robust water clarity algorithm than that developed from TOA reflectance.

Although we have not used near infrared and middle infrared wavelengths (band 4, 5 and 7) to predict water clarity in Río Tercero reservoir, the 6S model can remove the effects of atmospheric absorption caused by water vapor, carbon dioxide, ozone, methane, and other gases which reduce the apparent brightness of brighter surfaces (Vermote and Saleous, 2006; Sriwongsitanon et al., 2011). Table 5 shows that the corrected reflectance values of the near and middle infrared bands were higher than the uncorrected reflectance values. The average reflectance values of these bands tend to increase around 11% compared to the uncorrected values for the first image, around 18% for the second image, around 15% for the third image,

Table 5
Comparison of uncorrected and corrected reflectance values of each band and image.

ETM+ band	Average			Maximum			Standard deviation		
	U	C	%	U	C	%	U	C	%
May 14, 2004									
1	0.050	0.019	−62.3	0.457	0.490	7.3	0.032	0.035	10.3
2	0.069	0.044	−36.7	0.507	0.576	13.6	0.033	0.042	25.5
3	0.064	0.048	−25.6	0.451	0.518	14.9	0.036	0.045	24.3
4	0.248	0.278	12.1	0.986	0.996	1.0	0.065	0.079	20.4
5	0.190	0.209	10.4	0.596	0.686	15.2	0.053	0.063	19.0
7	0.120	0.134	11.7	0.645	0.723	12.1	0.051	0.062	21.6
September 28, 2006									
1	0.065	0.041	−37.2	0.415	0.467	12.3	0.021	0.026	22.5
2	0.081	0.079	−3.3	0.460	0.553	20.2	0.025	0.034	33.2
3	0.108	0.088	−18.7	0.418	0.498	19.0	0.035	0.045	28.9
4	0.194	0.227	17.2	0.972	0.996	2.5	0.041	0.051	24.6
5	0.257	0.302	17.5	0.559	0.659	17.9	0.067	0.081	20.8
7	0.184	0.222	20.7	0.698	0.784	12.3	0.057	0.069	21.1
September 7, 2010									
1	0.070	0.027	−61.0	0.505	0.573	13.3	0.020	0.020	0.6
2	0.084	0.065	−22.2	0.510	0.627	23.0	0.025	0.034	37.4
3	0.101	0.087	−14.2	0.463	0.573	23.6	0.034	0.046	34.4
4	0.178	0.198	11.3	0.889	0.965	8.5	0.043	0.054	25.5
5	0.242	0.281	16.1	0.634	0.753	18.8	0.066	0.081	22.0
7	0.240	0.283	17.9	0.885	0.956	8.0	0.055	0.068	23.6
November 10, 2010									
1	0.059	0.035	−40.3	0.337	0.369	9.4	0.023	0.027	16.4
2	0.083	0.074	−10.7	0.390	0.443	13.5	0.027	0.034	26.4
3	0.101	0.097	−3.7	0.357	0.400	11.9	0.040	0.049	22.8
4	0.223	0.252	12.9	0.740	0.835	12.9	0.039	0.046	18.2
5	0.258	0.288	11.3	0.484	0.545	12.7	0.067	0.077	16.4
7	0.244	0.278	13.9	0.676	0.785	16.1	0.055	0.064	16.4

U = uncorrected atmospheric effect; C = corrected atmospheric effect.

and around 13% for the fourth image. According to Sriwongsitanon et al. (2011), this is because the near infrared and middle infrared wavelengths are affected by atmospheric absorption while the influence of air molecules and aerosol particle scattering are negligible in these ranges. Since the 6S model can remove these effects, TOA reflectance values within these bands were then increased. Analyzing the maximum corrected reflectance values of all bands of the fourth images, an average increase of 13% within the range 1–24% was observed compared to the uncorrected reflectance values. The standard deviation of corrected reflectance values of all bands of all images increased within the range 1–37% with an average of around 22% compared to the uncorrected values of each band.

Like most previous remote sensing studies of limnological parameters, we focus on only one reservoir, but the transferability of the used methodologies and the general algorithm developed here to other environments remains unknown. However, similar characteristics of other aquatic systems of the region suggest that future research may allow the extension of such models to the regional scale, allowing the study of dynamics and trophic status of many surface waters that currently lack systematic studies of water quality in real and prospective time.

4. Conclusions

In this study, we have evaluated the potential of 6S radiative transfer model for atmospheric correction to improve reliability for estimating water clarity in Río Tercero reservoir. Pearson correlation coefficients and stepwise multiple regression analysis were used to identify the Landsat spectral bands or band ratios with and without atmospheric correction most correlated with SDT. Results shows that atmospheric corrected values of Landsat band 3 and the ratio 1/3 proved to be consistent predictors of water clarity in the reservoir. Using the 6S code we demonstrate the usefulness of atmospheric correction to Landsat data since water clarity algorithm using surface reflectance was more reliable than the TOA reflectance model.

The procedure presented here could become an independent, low additional training and low cost measurement tool for water management authorities and expands the possibilities of application in other aquatic systems with Landsat imagery or other existing sensors.

Acknowledgements

The authors thank editor and reviewers for their helpful comments on this manuscript. This work was supported by

SECyT-UNRC (Secretaría de Ciencia y Técnica, Universidad Nacional de Río Cuarto). Additional financial support was provided by CONICET (Consejo Nacional de Investigaciones Científicas y Técnicas).

References

Barsi, J.A., Schott, J.R., Palluconi, F.D., Hook, S.J., 2005. Validation of a web-based atmospheric correction tool for single thermal band instruments. In: Proceedings of Earth Observing Systems X, SPIE, Bellingham, United States.

Berk, A., Bernstein, L.S., Robertson, D.C., 1989. MODTRAN: a moderate resolution model for LOWTRAN 7. GL-TR-89-0122. Phillips Laboratory, Hanscom Air Force Base, MA.

Bonansea, M., Fernandez, R.L., 2013. Remote sensing of suspended solid concentration in a reservoir with frequents wildland fires on its watershed. Water Sci. Technol. 67 (1), 217–223.

Bonansea, M., Ledesma, C., Rodriguez, C., Pinotti, L., 2015. Water quality assessment using multivariate statistical techniques in Río Tercero reservoir, Argentina. Hydrol. Res. 46 (3), 377–387.

Brezonik, P., Menken, D., Bauer, M., 2005. Landsat-based remote sensing of lake water quality characteristics, including chlorophyll and colored dissolved organic matter (CDOM). Lake Reservoir Manage. 21 (4), 373–382.

Chander, G., Markham, B.L., Helder, D.L., 2009. Summary of current radiometric calibration coefficients for Landsat MSS, TM, ETM+, and EO− 1 ALI sensors. Remote Sens. Environ. 113 (5), 893–903.

Chao Rodríguez, Y., el Anjoumi, A., Domínguez Gómez, J.A., Rodríguez Pérez, D., Rico, E., 2014. Using Landsat image time series to study a small water body in Northern Spain. Environ. Monit. Assess. 186 (6), 3511–3522.

Chernetskiy, M., Shevyrnogov, A., Shevnina, S., Vysotskaya, G., Sidko, A., 2009. Investigations of the Krasnoyarsk reservoir waters based on the multispectral satellite data. Adv. Space Res. 43 (2), 206–213.

Cohen, W.B., Goward, S.N., 2004. Landsat's role in ecological applications of remote sensing. Biosci. 54 (6), 535–545.

Cox, R.M., Forsythe, R.D., Vaughan, G.E., Olmsted, L.L., 1998. Assessing water quality in the Catawba river reservoirs using Landsat thematic mapper satellite data. Lake Reservoir Manage. 14, 405–416.

Cózar, A., García, C.M., Gálvez, J.A., Loiselle, S.A., Bracchini, L., Cognetta, A., 2005. Remote sensing imagery analysis of the lacustrine system of Ibera wetland (Argentina). Ecol. Model. 186 (1), 29–41.

Dekker, A.G., Peters, S.W.M., 1993. The use of the thematic mapper for the analysis of eutrophic lakes: a case study in the Netherlands. Int. J. Remote Sens. 14, 799–821.

Domínguez Gómez, A., Chuvieco Salinero, E., Sastre Merlín, A., 2009. Monitoring transparency in inland water bodies using multispectral images. Int. J. Remote Sens. 30, 1567–1586.

Doña, C., Sánchez, J.M., Caselles, V., Antonio Dominguez, J., Camacho, A., 2014. Empirical relationships for monitoring water quality of lakes and reservoirs through multispectral images. IEEE J. Sel. Top. Appl. Earth Obs. Remote Sens. 7 (5), 1632–1641.

Fernandez, R.L., Bonansea, M., Cosavella, A., Monarde, F., Ferreyra, M., Bresciano, J., 2012. Effects of bubbling operations on a thermally stratified reservoir: implications for water quality amelioration. Water Sci. Technol. 66 (12), 2722–2730.

Fernandez, R.L., Bonansea, M., Marques, M., 2014. Monitoring turbid plume behavior from Landsat imagery. Water Resour. Manage. 28 (10), 3255–3269.

Hellweger, F.L., Schlosser, P., Lall, U., Weisse, J.K., 2004. Use of satellite imagery for water quality studies in New York harbor. Estuarine Coastal Shelf Sci. 61, 437–448.

Hu, C., Muller-Karger, F.E., Andrefouet, S., Carder, K.L., 2001. Atmospheric correction and cross-calibration of LANDSAT-7/ETM + imagery over aquatic environments: a multiplatform approach using seaWiFS/MODIS. Remote Sens. Environ. 78 (1–2), 99–107.

Huang, C., Zhang, Z., Yang, L., Luylie, B., Homer, C., 2002. MRLC 2000. Image Preprocessing Procedure. USGS White paper.

Irish, R.R., 1998. Landsat 7 science data user's handbook. NASA, Goddard Space Flight Center, Greenbelt, Maryland.

Ji, L., Zhang, L., Wylie, B., 2009. Analysis of dynamic thresholds for the normalized difference water index. Photogramm. Eng. Remote Sens. 75 (11), 1307–1317.

Karakaya, N., Evrendilek, F., Aslan, G.R., Gungor, K., Karakas, D., 2011. Monitoring of lake water quality along with trophic gradient using Landsat data. Int. J. Environ. Sci. Technol. 8 (4), 817–822.

Kneizys, F.X., Shettle, E.P., Abreu, L.W., Chetwynd, J.H., Anderson, G. P., Gallery, W.O., Selby, J.E.A., Clough, S.A., 1988. User's Guide to LOWTRAN 7, Air Force Geophysics Laboratory, Hanscom AFB Environmental Research Report ERP No. 1010.

Kloiber, S.M., Brezonik, P.L., Bauer, M.E., 2002a. Application of Landsat imagery to regional-scale assessments of lake clarity. Water Res. 36, 4330–4340.

Kloiber, S.M., Brezonik, P.L., Olmanson, L.G., Bauer, M.E., 2002b. A procedure for regional lake water clarity assessment using Landsat multispectral data. Remote Sens. Environ. 82 (1), 38–47.

Kulkarni, A., 2011. Water quality retrieval from Landsat TM imagery. Procedia Comput. Sci. 6, 475–480.

Lamaro, A.A., Mariñelarena, A., Torrusio, S.E., Sala, S.E., 2013. Water surface temperature estimation from Landsat 7 ETM+ thermal infrared data using the generalized single-channel method: case study of Embalse del Río Tercero (Córdoba, Argentina). Adv. Space Res. 51 (3), 492–500.

Lathrop, R.G., Lillesand, T.M., 1986. Use of thematic mapper data to assess water quality in Green Bay and Central Lake Michigan. Photogramm. Eng. Remote Sens. 52, 671–680.

Lathrop, R.G., 1992. Landsat thematic mapper monitoring of turbid inland water quality. Photogramm. Eng. Remote Sens. 58, 465–470.

Lavery, P., Pattiaratchi, C., Wyllie, A., Hick, P., 1993. Water quality monitoring in estuarine waters using the Landsat thematic mapper. Remote Sens. Environ. 46, 268–280.

Ledesma, C., Bonansea, M., Rodríguez, C., Delgado, A.R.S., 2013. Water quality control in Río Tercero reservoir (Argentina) using geographical information systems and linear regression models. Rev. Ambiente Agua. 8 (2), 67–76.

Loveland, T.R., Dwyer, J.L., 2012. Landsat: building a strong future. Remote Sens. Environ. 122, 22–29.

Mahiny, A.S., Turner, B.J., 2007. A comparison of four common atmospheric correction methods. Photogramm. Eng. Remote Sens. 73 (4), 361–368.

Mariazzi, A.A., Donadelli, J.L., Arenas, P., Di Siervi, M.A., Bonetto, C., 1992. Impact of a nuclear power plant on water quality of Embalse del Río Tercero reservoir (Córdoba, Argentina). Hidrobiologia 246, 129–140.

Masek, J.G., Vermote, E.F., Saleous, N.E., Wolfe, R., Hall, F.G., Huemmrich, K.F., Gao, F., Kutler, J., Lim, T.K., 2006. A Landsat surface reflectance dataset for North America, 1990–2000. IEEE Geosci. Remote Sens. Lett. 3 (1), 68–72.

Matthews, M.W., 2011. A current review of empirical procedures of remote sensing in inland and near-coastal transitional waters. Int. J. Remote Sens. 32 (21), 6855–6899.

McCullough, I.M., Loftin, C.S., Sader, S.A., 2012a. Combining lake and watershed characteristics with Landsat TM data for remote estimation of regional lake clarity. Remote Sens. Environ. 123, 109–115.

McCullough, I.M., Loftin, C.S., Sader, S.A., 2012b. High-frequency remote monitoring of large lakes with MODIS 500 m imagery. Remote Sens. Environ. 124, 234–241.

McFeeters, S.K., 1996. The use of normalized difference water index (NDWI) in the delineation of open water features. Int. J. Remote Sens. 17, 1425–1432.

Mukherjee, S., Joshi, P.K., Garg, R.D., 2014. A comparison of different regression models for downscaling Landsat and MODIS land surface temperature images over heterogeneous landscape. Adv. Space Res. 54 (4), 655–669.

Onderka, M., Pekárová, P., 2008. Retrieval of suspended particulate matter concentrations in the Danube river from Landsat ETM data. Sci. Total Environ. 397 (1), 238–243.

Oguro, Y., Suga, Y., Takeuchi, S., Ogawa, H., Tsuchiya, K., 2003. Monitoring of a rice field using Landsat-5 TM and Landsat-7 ETM+ data. Adv. Space Res. 32 (11), 2223–2228.

Olmanson, L.G., Bauer, M.E., Brezonik, P.L., 2008. A 20-year Landsat water clarity census of Minnesota's 10,000 lakes. Remote Sens. Environ. 112 (11), 4086–4097.

Ouaidrari, H., Vermote, E.F., 1999. Operational atmospheric correction of Landsat TM data. Remote Sens. Environ. 70, 4–15.

Rahman, H., Dedieu, G., 1994. SMAC: a simplified method for atmospheric correction of satellite measurements in the solar spectrum. Int. J. Remote Sens. 15 (1), 123–143.

Sharma, A.R., Badarinath, K.V.S., Roy, P.S., 2009. Comparison of ground reflectance measurement with satellite derived atmospherically corrected reflectance: a case study over semi-arid landscape. Adv. Space Res. 43 (1), 56–64.

Song, C., Woodcock, C.E., Seto, K.C., Lenney, M.P., Macomber, S.A., 2001. Classification and change detection using Landsat TM data: when and how to correct atmospheric effects? Remote Sens. Environ. 75 (2), 230–244.

Sriwongsitanon, N., Surakit, K., Thianpopirug, S., 2011. Influence of atmospheric correction and number of sampling points on the accuracy of water clarity assessment using remote sensing application. J. Hydrol. 401 (3–4), 203–220.

Tachiiri, K., 2005. Calculating NDVI for NOAA/AVHRR data after atmospheric correction for extensive images using 6S code: a case study in the Marsabit district, Kenya. ISPRS J. Photogramm. Remote Sens. 59 (3), 103–114.

Takashima, T., Masuda, K., 2000. Atmospheric correction for the satellite visible data over heterogeneous surfaces. Appl. Math. Comput. 116, 181–196.

Tebbs, E.J., Remedios, J.J., Harper, D.M., 2013. Remote sensing of chlorophyll-a as a measure of cyanobacterial biomass in Lake Bogoria, a hypertrophic, saline–alkaline, flamingo lake, using Landsat ETM+. Remote Sens. Environ. 135, 92–106.

Trivero, P., Borasi, M., Biamino, W., Cavagnero, M., Rinaudo, C., Bonansea, M., Lanfri, S., 2013. River pollution remediation monitored by optical and infrared high-resolution satellite images. Environ. Monit. Assess. 185 (9), 7647–7658.

USGS. Phase 2 gap-fill algorithm: SLC-off gap-filled products gap-fill algorithm methodology, 2004. Available from http://landsat.usgs.gov/documents/L7SLCGapFilledMethod.pdf [Accessed September 23, 2014].

Vermote, E.F., Tanre, D., Deuze, J.L., Herman, M., Morcrette, J.J., 1997. Second simulation of the satellite signal in the solar spectrum, 6S: an overview. IEEE Trans. Geosci. Remote Sens. 35, 675–686.

Vermote, E.F., Saleous, N.Z., 2006. Operational atmospheric correction of MODIS visible to middle infrared land surface data in the case of an infinite lambertian target. In: Qu, J. et al. (Eds.), Earth Sci. Satell. Remote Sens. l(8), pp. 123–153.

Vincent, R.K., Qin, X., McKay, R.M., Miner, J., Czajkowski, K., Savino, J., Bridgemand, T., 2004. Phycocyanin detection from LANDSAT TM data for mapping cyanobacterial blooms in Lake Erie. Remote Sens. Environ. 89 (3), 381–392.

Xu, H., Huang, S., Zhang, T., 2013. Built-up land mapping capabilities of the ASTER and Landsat ETM+ sensors in coastal areas of southeastern China. Adv. Space Res. 52 (8), 1437–1449.

Zhao, D., Cai, Y., Jiang, H., Xu, D., Zhang, W., An, S., 2011. Estimation of water clarity in Taihu Lake and surrounding rivers using Landsat imagery. Adv. Water Resour. 34 (2), 165–173.

Zhao, W., Takahashi, H., Tamuara, M., 1999. Atmospheric and spectral correction of Landsat TM data to estimate wetland surface albedo – a case study of Kushiro Mire, Hokkaido. Japan. Int. Peat J. 9, 11–20.

Zhao, W., Tamura, M., Takahashi, H., 2000. Atmospheric and spectral corrections for estimating surface albedo from satellite data using 6S code. Remote Sens. Environ. 76 (2), 202–212.